A Spatial–Spectral Adaptive Haze Removal Method for Visible Remote Sensing Images

Huanfeng Shen, *Senior Member, IEEE*, Chi Zhang, Huifang Li, *Member, IEEE*, Quan Yuan, and Liangpei Zhang, *Fellow, IEEE*

***Abstract*— Visible remotely sensed images usually suffer from the haze, which contaminates the surface radiation and degrades the data quality in both spatial and spectral dimensions. This study proposes a spatial–spectral adaptive haze removal method for visible remote sensing images to resolve spatial and spectral problems. Spatial adaptation is considered from global and local aspects. A globally nonuniform atmospheric light model is constructed to depict spatially varied atmospheric light. Moreover, a bright pixel index is built to extract local bright surfaces for transmission correction. Spectral adaptation is performed by exploring the relationships between image gradients and transmissions among bands to estimate spectrally varied transmission. Visible remote sensing images featuring different land covers and haze distributions were collected for synthetic and real experiments. Accordingly, four haze removal methods were selected for comparison. Visually, the results of the proposed method are completely free from haze and colored naturally in all experiments. These outcomes are nearly the same as the ground truth in the synthetic experiments. Quantitatively, the mean-absolute-error, root-mean-square-error, and spectral angle are the smallest, and the coefficient-of-determination (R^2) is the largest among the five methods in the synthetic experiments. R^2, structural similarity index measure, and the correlation coefficient between the result of the proposed method and the reference image are closest to 1 in the real data experiments. All experimental analyses demonstrate that the proposed method is effective in removing haze and recovering ground information faithfully under different scenes.**

***Index Terms*— Bright pixel index (BPI), dark channel prior (DCP), haze removal, spatial–spectral adaptive.**

I. Introduction

DURING the acquisition of Earth's surface information by satellite imaging systems, radiation undergoes a complicated process through the path of sun–atmosphere–Earth's surface–atmosphere–sensor [1]. Radiative transfer mostly occurs in the atmosphere, which inevitably affects the accuracy of the recorded ground information [2]. Haze is a typical type of turbid atmosphere that consists of small dust particles or liquid droplets and occurs frequently [3]. Scattering triggered by these turbid particles causes radiance distortion in the spatial and spectral dimensions for remote sensing images, particularly in the visible bands owing to the short wavelengths, thereby resulting in difficult image interpretation and inversion. Therefore, haze removal should be conducted and the ground information for a hazy visible image should be restored.

Several methods that have been proposed to implement haze removal can be grouped into two categories, namely multiimage- and single-image-based methods. Multiimage-based methods remove haze by utilizing complementary information from other temporal or spectral images [4]–[9]. For these types of methods, the requirements for the reference data limit their generalization, and the available ground information in the original hazy region is not fully utilized. By contrast, single-image-based methods maximize the information from hazy images to remove haze, which is considerably general but challenging. This study focuses on single-image-based methods.

In general, the single-image-based haze removal methods comprise the radiative transfer model (RTM) [10]–[15] and statistical information-based methods [16]–[36]. On the one hand, RTM-based methods require the simultaneous atmospheric property-related parameters, which are often unavailable and difficult to obtain accurately. Moreover, RTMs substantially focus on the global vertical variation rather than the local horizontal variation of the atmosphere, such as haze. To overcome this shortcoming, Liang *et al.* [14], [15] proposed to build a lookup table to obtain the horizontally varied aerosol optical depth (AOD). However, land covers were initially required, which is also a problem for many hazy visible images.

On the other hand, statistical information-based methods mainly utilize the image characteristics of haze to realize the removal, which is independent of the atmospheric parameters and models. These methods can be divided into three classes: frequency domain—[16], [17], spectral transformation—[18]–[25], and dark pixel-based methods—[26]–[36]. First, haze can be removed in the frequency domain by suppressing and enhancing low- and high-frequency information, respectively. However, the valid low-frequency information will be

Manuscript received June 1, 2019; revised January 1, 2020; accepted February 4, 2020. This work was supported by the National Natural Science Foundation of China under Grant 41871246, Grant 41631180, Grant 41971303, and Grant 61671334. *(Corresponding author: Huifang Li.)*

Huanfeng Shen is with the School of Resource and Environmental Sciences, Wuhan University, Wuhan 430072, China, and also with the Collaborative Innovation Center for Geospatial Technology, Wuhan University, Wuhan 430072, China (e-mail: shenhf@whu.edu.cn).

Chi Zhang and Huifang Li are with the School of Resource and Environmental Sciences, Wuhan University, Wuhan 430072, China (e-mail: zhangchi9502@outlook.com; huifangli@whu.edu.cn).

Quan Yuan is with Guangdong OPPO Mobile Telecommunications Corporation, Ltd, Dongguan 523000, China (e-mail: 1127905893@qq.com).

Liangpei Zhang is with the State Key Laboratory of Information Engineering in Surveying, Mapping and Remote Sensing, Wuhan University, Wuhan 430079, China (e-mail: zlp62@whu.edu.cn).

Color versions of one or more of the figures in this article are available online at http://ieeexplore.ieee.org.

Digital Object Identifier 10.1109/TGRS.2020.2974807

inevitably damaged or lost while haze is being removed. Second, spectral transformation-based methods take advantage of the radiance differences of the ground and haze between bands to detect and remove haze. Representative spectral transformations include haze optimized transformation (HOT) [18]–[20], tasseled cap transformation [21], [22], and component analysis [23], [24]. In those transformation-based methods, all pixels, including the hazy and clear ones, are altered, thereby resulting in the frequent appearance of radiation distortion. Third, dark pixel-based methods are ancient and meanwhile developed. The primary one is the dark object subtraction (DOS) [26], in which the value of the dark object represents the influence of the atmosphere in each band. On the basis of this idea, some new haze removal methods, such as an improved DOS technique [27], haze thickness map-based method [28], and dark channel prior (DCP)-based method [29], have been developed by searching the dark pixel globally or locally in a band or in multiple bands. Global operation is usually suitable for globally invariant haze, whereas local operation is appropriate for spatially varied haze. Moreover, searching in multiple bands provides a higher probability for the existence of dark pixels than merely searching in one band. DCP is constructed on the basis of local searching in multiple bands for haze removal in close shot images. Given the validity of DCP, some DCP-based haze removal methods for remote sensing images have been proposed and improved [30]–[36].

In general, dark pixel-based methods are effective in removing haze and maintaining clear regions. To date, these methods have been the most commonly used haze removal methods. However, note that the existence of dark pixels is the key to realizing total haze removal. Once the dark pixel is absent (e.g., in bright soils), the concerned region would be mistaken as haze and overcorrection would occur thereafter [29]. Different bands are often processed individually or equally, disregarding the correlation of haze between bands, which is also a problem for the other type of statistical information-based methods. The band-by-band operation is the main reason for the spectral distortion in the haze removal results [27].

To overcome the overcorrection and spectral distortion shortcomings, this study proposes a spatial–spectral adaptive haze removal method for visible remote sensing images. Spatial adaptation is conducted by considering varied atmospheric light and bright surfaces. Spectral adaptation is performed by estimating the band varied transmission. The remainder of this article is organized as follows. Section II briefly describes the hazy image model and DCP. Section III provides the details of the proposed haze removal method. Section IV presents the experimental results and comparative analysis. Lastly, Section V summarizes this article.

II. Background

A. Hazy Image Model

Radiation interacts with the land surface and turbid atmosphere before it reaches the sensor, as illustrated in Fig. 1.

To describe the imaging process, a widely used hazy image model has been proposed, which can be expressed as follows [37]–[40]:

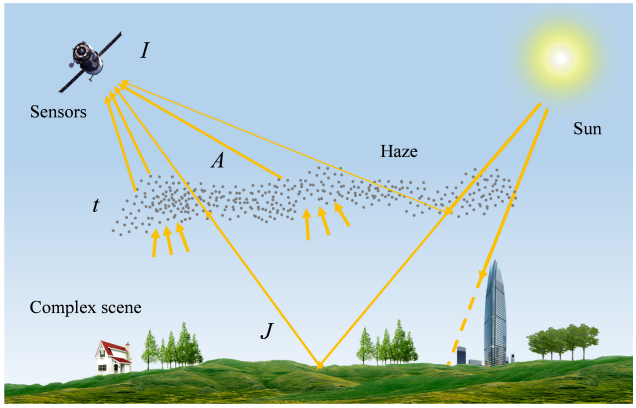

Fig. 1. Illustration of radiation transfer under a turbid atmosphere.

$$I(x) = J(x)t(x) + A(1 - t(x)) \tag{1}$$

where x is the position of the pixel in the image; I is the observed image; t is the transmission, indicating the portion of ground radiance that reaches the sensor; A is the atmospheric light, which is a constant when the atmospheric scattering intensity is uniform [38]; and J denotes the clear image. The goal of haze removal is to initially estimate A and t from I, and recover J thereafter according to the model.

B. Dark Channel Prior

DCP describes a statistical law, which states that the intensity of some pixels in nonsky local patches will be extremely low and tends to zero in at least one or several bands for clear images [29]. For an arbitrary image J, its dark channel can be calculated by using two minimum operators

$$J^{\text{dark}} = \min_{\Omega(x)} \left(\min_{c \in \{\text{r,g,b}\}} J^c(x) \right) \tag{2}$$

where c represents the visible bands of J, $\Omega(x)$ is the local window centered at x, $\min_{c \in \{\text{r,g,b}\}}$ is the minimum operator performed on each pixel, $\min_{\Omega(x)}$ is a minimum filter with window size $\Omega(x)$, and J^{dark} represents the dark channel of image J.

By coupling the hazy image model and DCP, the key parameter (i.e., transmission) can be estimated as follows:

$$t = \frac{1 - \hat{I}^{\text{dark}}}{1 - \hat{J}^{\text{dark}}} \tag{3}$$

where $\hat{I}$ and $\hat{J}$ are the images of I and J, respectively, normalized by A; and $\hat{I}^{\text{dark}}$ and $\hat{J}^{\text{dark}}$ represent the dark channel of $\hat{I}$ and $\hat{J}$, respectively. When dark pixel exists in the local patch, the transmission can be estimated correctly. Otherwise, the transmission will be underestimated, which will cause color distortion.

III. Method

Haze in remote sensing images shows several prominent characteristics, covers a large area, holds high radiance, gradually changes in space, and varies among bands. Dark pixels

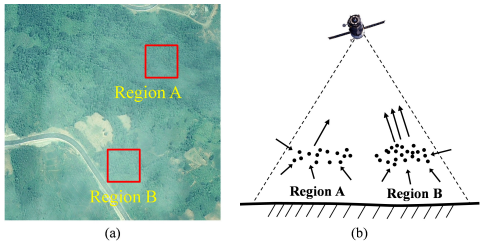

Fig. 2. Illustration of the heterogeneity of atmospheric scattering in a large scene. (a) Uneven haze-covered image. (b) Atmospheric scattering intensity in regions A and B.

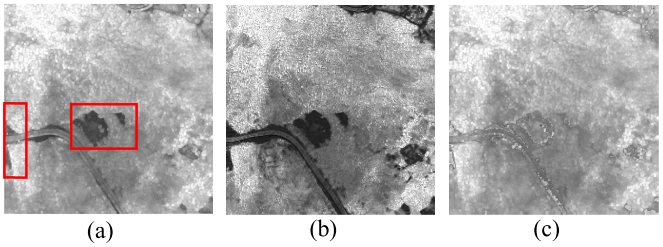

Fig. 3. Example of spatially adaptive transmission correction. (a) Original transmission. (b) BPI. (c) Spatially corrected transmission.

can be found in remote sensing images, thereby ensuring the availability of DCP for remote sensing haze removal. However, numerous bright surfaces are distributed on Earth, where dark pixels are lacking, thereby making DCP invalid in some regions. Only one transmission can be directly estimated by DCP, neglecting the haze effects variation among bands. The neglect causes insufficient correction to appear in some bands, thereby leading to the final color distortion. To solve these problems, this study proposes an adaptive haze removal method from the spatial and spectral aspects.

A. Spatial Adaptive Processing

1) Nonuniform Atmospheric Light Estimation: Previous studies have often assumed that atmospheric light is constant for a scene. This assumption is true for the majority of close-shot images because the atmospheric scattering intensity in images is stable [38]. However, for remote sensing images with broad imaging range, the scattering intensity varies spatially (see Fig. 2). The haze in region B is thicker than that in region A [see Fig. 2(a)], thereby indicating that the corresponding scattering intensity is different, as illustrated in Fig. 2(b). In general, the larger the scene, the more uneven the scattering intensity. Therefore, an atmospheric light estimation algorithm should be developed to depict the heterogeneity of atmospheric scattering for a large scene.

For remote sensing images, we take the general atmospheric light as basis and variation as an increment to estimate nonuniform atmospheric light. Thereafter, the nonuniform atmospheric light A_{nua} can be expressed as follows:

$$A_{\text{nua}} = A_{\text{basis}} + \Delta A_{\text{local}} \tag{4}$$

where A_{basis} and ΔA_{local} are the general atmospheric light and increment of the atmospheric light, respectively.

The general atmospheric light A_{basis} reflects the atmospheric light of the global scene, which can be estimated according to the solution proposed by He *et al.* [29]. The increment describes the difference between the local and global scenes, which can be estimated through the background brightness of images. The low-frequency portion of images is commonly taken to represent the background brightness of such images and is calculated in this study using Gaussian low-pass filter. In addition, a minimum filter is adopted to ensure that the atmospheric light in a local region is stable. Hence, the increment can be expressed as follows:

$$\Delta A_{\text{local}} = \min_{\Psi} \tilde{I} - \tilde{I}_{\min} \tag{5}$$

where $\tilde{I}$ is the background brightness of an image, $\tilde{I}_{\min}$ is the minimum value of $\tilde{I}$, and $\min_{\Psi}$ is a minimum filter with window Ψ. The window size is initialized by visually measuring the spatial variation of haze, and determined thereafter by interacting with the results. In general, the more uniform the haze, the larger the initialization window size should be. Moreover, ΔA_{local} is the estimated atmospheric light increment.

2) Transmission Correction for Bright Surfaces: As there is a lack of dark pixels in bright surfaces, the transmission of these regions will likely be underestimated, as shown in the red rectangles marked in Fig. 3(a). To solve this problem, a bright pixel identification algorithm is proposed to extract the underestimated transmission. Thereafter, an adaptive correction function is applied to revise the transmission.

For a bright pixel, the color is often white. This phenomenon indicates that the intensity in each band is extremely high, whereas the differences are extremely small between bands. These characteristics are used as bases to construct the following bright pixel identification algorithm called bright pixel index (BPI):

$$\text{BPI}(x) = \frac{\max\limits_{c\in\{\text{r,g,b}\}} I^c(x) - \min\limits_{c\in\{\text{r,g,b}\}} I^c(x)}{\min\limits_{c\in\{\text{r,g,b}\}} I^c(x)} \tag{6}$$

where $\max\limits_{c\in\{\text{r,g,b}\}} I^c(x)$ and $\min\limits_{c\in\{\text{r,g,b}\}} I^c(x)$ denote the maximum and minimum of x, respectively, among the visible bands c. In general, bright pixels have a low BPI value [see Fig. 3(b)]. The bright pixels can be identified by setting a suitable threshold for BPI.

To correct the transmission for bright pixels, a correction coefficient C is introduced to obtain the surface-adaptive transmission $\tilde{t}$, which can be expressed as follows:

$$\tilde{t}(x) = \begin{cases} t(x), & x \notin \Phi \\ \min(C(x)\cdot t(x), t_0), & x \in \Phi \end{cases} \tag{7}$$

where Φ is the set of bright pixels. Theoretically, the transmission is between 0 and 1, while its value in the bright surface may exceed 1 after revision. Hence, an upper bound $t_0 = 0.95$ is set to restrict the value. The reason for setting this value is that the dark channel intensity considerably approximates 0 but larger than that in remote sensing images.

That is, the transmission of the visually clear atmosphere is slightly below 1.

The problem is about calculating C. If the bright pixel holding the lowest value in the dark channel is assumed to be clear, then its corresponding transmission should be equal to 1. Thereafter, (3) indicates that the corresponding correction coefficient for this pixel can be calculated as follows:

$$C_m = \frac{1}{1 - \min\limits_{x\in\Phi} \hat{I}(x)^{\text{dark}}} \tag{8}$$

where $\min\limits_{x\in\Phi} \hat{I}(x)^{\text{dark}}$ is the minimum value in the dark channel among the bright pixels. As the intensity of a bright pixel increases, the transmission will be further underestimated, which means that the corresponding correction coefficient should be larger. In addition, the relationship between the real and underestimated transmissions is an inverse proportional function related to the dark channel. Therefore, to ensure that the corrected transmission is as close as possible to the real situation, an adaptive function is constructed to stretch C_m, which can be expressed as follows:

$$C(x) = \frac{\max\limits_{x\in\Phi} \hat{I}(x)^{\text{dark}} - \min\limits_{x\in\Phi} \hat{I}(x)^{\text{dark}}}{\max\limits_{x\in\Phi} \hat{I}(x)^{\text{dark}} - \hat{I}(x)^{\text{dark}}} \cdot C_m \tag{9}$$

where $\max\limits_{x\in\Phi} \hat{I}(x)^{\text{dark}}$ is the maximum of the dark channel among the bright pixels, and C denotes the correction coefficient. After the adaptive correction strategy is adopted, the underestimated transmission can be refined [see Fig. 3(c)].

B. Spectral Adaptive Processing

Atmospheric scattering law states that haze effects vary in different bands [27], thereby indicating that transmission is wavelength-dependent. Concretely, the longer the wavelength, the larger the transmission. However, the difference in transmission between bands is often disregarded, resulting in the incomplete removal of haze in short-wavelength bands. To clear the haze in each visible band, a gradient-based spectral adaptive processing procedure is proposed.

In general, the influence of haze is twofold: it increases brightness and reduces gradient [16]. Brightness can be attributed to haze cover or high reflectance of the land surface. Thus, brightness is not a distinctive feature of haze. On the contrary, the blur effect of haze is independent of land cover, and can be expressed by the image gradient describing the relative relationship among pixels. As wavelength increases, the blur influence becomes weaker and the gradient higher.

Evidently, gradient and transmission reflect the influence of haze and are positively related to wavelength. Therefore, it is natural to surmise that the two variables are correlated. To verify this assumption, 500 subimages with a size of 200 × 200 pixels were cropped from different images. After normalization, the gradient of each band was calculated and fit thereafter with the transmission. In particular, gradient and transmission are represented by their average values, which are denoted as $\bar{G}$ and $\bar{t}$, respectively. The results of this experiment indicate that the gradient of the red band and the transmission

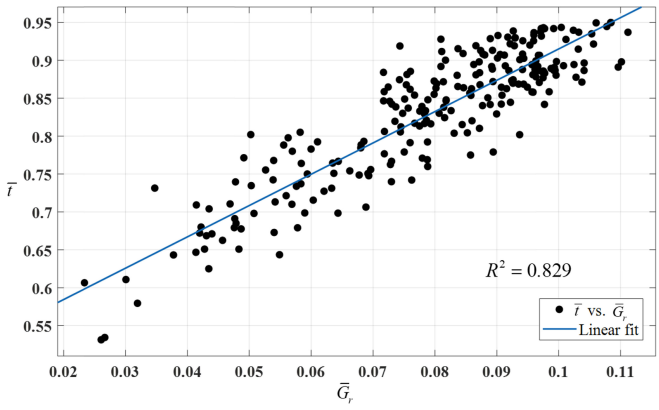

Fig. 4. Linear fitting between the gradient $\bar{G}_r$ and the transmission $\bar{t}$.

show the closest linear correlation, with $\boldsymbol{R^2}$ reaching 0.829, as illustrated in Fig. 4.

This result proves that the linearity between the two variables is universal and significant, which can be modeled as follows:

$$\bar{t} = a \cdot \bar{G}_r + b \tag{10}$$

where a and b are the fitting coefficients.

Given the high correlation between the visible bands, the presumption is that the linearity relationship in (10) is also suitable for the other visible bands. Therefore, the relative relationship of the transmission between visible bands can be determined by their average gradient. Note that (10) is inadaptable to near-infrared or longer wavelengths because of the lack of a high correlation between visible and near-infrared or longer wavelengths. In addition, the statistics of the sources of dark pixels was performed, and that the majority of the dark pixels are from the red band of a hazy image and a few are from other visible bands. Thus, the spatially corrected transmission is considered suitable for removing haze in the red band. Therefore, the transmission of each visible band is given as follows:

$$t_r = \tilde{t} \quad t_g = \frac{a \cdot \bar{G}_g + b}{a \cdot \bar{G}_r + b} \cdot \tilde{t} \quad t_b = \frac{a \cdot \bar{G}_b + b}{a \cdot \bar{G}_r + b} \cdot \tilde{t} \tag{11}$$

where $\bar{G}_g$ and $\bar{G}_b$ represent the average gradient of the green and blue bands, respectively, and t_i indicates the transmission of band i. Given that the derived transmission is merely an approximation, a guided filter is introduced to avoid some halo and block artifacts and to obtain the final band-varying transmission.

IV. Experiments

To validate the effectiveness of the proposed method, several visible remote sensing images selected from different scenes were collected for synthetic and real experiments. Four haze removal methods, including HOT [18], fast visibility restoration (FVR) [40], traditional DCP (TDCP) [29], and dark channel-saturation prior (DSP) methods [34], were compared with the proposed method. For a fair comparison, the optimal parameters used in these methods were determined

using iterative adjustment. Four indexes, namely, mean-absolute-error (MAE), coefficient-of-determination ($\boldsymbol{R}^2$), root-mean-square-error (RMSE), and spectral angle (SA), were calculated to measure the haze removal results in the synthetic experiments. Visual assessments were performed in real experiments. For the quantitative assessment, $\boldsymbol{R^2}$, structural similarity index measure (SSIM), and correlation coefficient (CC) were calculated by taking a clear image with a minimal time difference as reference.

A. Parameter Design for Comparison Methods

Four methods, namely, HOT, FVR, TDCP, and DSP, were chosen for comparison. For HOT, the hierarchical interval l used to slice the HOT map is the key parameter. The smaller the l, the more complete the haze removal. To obtain clean results, l is set to 1. For FVR, the percentage of restoration p, white balance level b, the maximum size of the white objects sv, maximum window size for the adapted filtering si, and gamma correction intensity g are the five parameters affecting the results. p is set to 1 to restore the image completely. Tarel and Hautiere [40] suggested that b is set to 0.5 and sv is set as follows:

$$sv = 2\frac{\max(m,n)}{50} + 1 \tag{12}$$

where m and n are the sizes of the input image. si is used for softening the noise. Experiments indicate that 50 is a suitable value. To maintain the spectra of clear regions, g is set to 1. For TDCP, the key parameter is the window size w. By testing different w for each image, the optimal sizes shown in Figs. 5–10 are 7×7, 5×5, 13×13, 5×5, 17×17, and 7×7, respectively. For DSP, the haze removal procedure is adaptive, and no parameter is required to be set manually. These algorithms run on a Windows 10 operating system using a 3.0-GHz Intel Core i5-8500 processor.

B. Synthetic Experiments

The generation of synthetic hazy images was based on the hazy image model expressed in (1). J was the selected clear image (i.e., ground truth). The atmospheric light A was estimated from a real hazy image via the nonuniform atmospheric light model. The transmission in the red band t_r was calculated using DCP. The transmission in the other visible bands was derived using the scattering law, which can be expressed as follows [29]:

$$t_i = t_r^{\left(\frac{\lambda_r}{\lambda_i}\right)^{\gamma}} \tag{13}$$

where λ is the central wavelength, the subscript r denotes the red band, i represents the green or blue band, and γ is the variable varying from 0 to 4. Once the A and band-varied t are obtained, the hazy image is synthetized.

Figs. 5 and 6 show two synthetic hazy images with different spatial resolutions and the corresponding haze removal results.

Fig. 5(g) shows a clear image with 30-m spatial resolution cropped from Landsat-8 Operational Land Imager (OLI). Fig. 5(a) illustrates a synthetic hazy image, in which the haze shows significant spatial variation. Fig. 5(b)–(f) show the results of HOT, FVR, TDCP, DSP, and the proposed method, respectively. Visually, HOT successfully removes haze over the full scene but presents evident color distortion, which is extremely different from the ground truth. In the result of FVR, most haze can be removed but residuals remain. Moreover, bare soils are dark compared with the ground truth, which can be attributed to the overcorrection in these regions. In Fig. 5(d), part of haze remains and the overcorrection appears at some regions, thereby suggesting that TDCP cannot considerably handle spatially varied haze and bright surfaces. Furthermore, the corrected regions look bluish owing to the insufficient correction for the green and blue bands. As a result, DSP shows that the image is partially free from haze and with a higher brightness than the ground truth. The reason is that the saturation prior used in DSP is minimally valid in such an image, thereby leading to the overestimation of transmission and undercorrection of the result. The result of the proposed method indicates that the image details are substantially retrieved and the color is closer to the ground truth visually compared with the other results. Overall, the proposed method outperforms the compared methods in terms of haze removal and color fidelity by visual assessment.

TABLE I
QUANTITATIVE ASSESSMENT OF DIFFERENT RESULTS

	HOT	FVR	TDCP	DSP	Proposed
MAE	11.4153	17.9156	9.7371	12.0504	**1.5298**
$\boldsymbol{R}^2$	0.7193	0.5900	0.8304	0.6012	**0.9477**
RMSE	11.8321	19.4861	10.6673	13.7567	**2.1304**
SA	3.7637	2.5334	2.2904	2.5217	**0.5872**

To measure the proposed method quantitatively, four metrics, MAE, RMSE, $\boldsymbol{R}^2$, and SA, were selected. Their definitions are as follows [41], [42]:

$$\text{MAE} = \frac{1}{n}\sum_{i=1}^{n} |\hat{J}_i - J_i| \tag{14}$$

$$\text{RMSE} = \sqrt{\frac{\sum_{i=1}^{n}\left(\hat{J}_i - J_i\right)^2}{n}} \tag{15}$$

where i is the pixel index, n is the total pixels, $\hat{J}$ is the ground truth, and J is the corrected result

$$R^2 = \frac{\sum_{i=1}^{n}\left(\hat{J}_i - \bar{J}\right)^2}{\sum_{i=1}^{n}\left(J_i - \bar{J}\right)^2} \tag{16}$$

where $\bar{J}$ is the mean value of J

$$\text{SA} = \frac{1}{n}\sum_{i=1}^{n}\cos^{-1}\left(\frac{\hat{J}_i^T J_i}{\sqrt{J_i^T J_i}\sqrt{\hat{J}_i^T \hat{J}_i}}\right) \tag{17}$$

where the superscript T denotes the transpose operator.

Table I lists the statistical results of these metrics. As indicated by MAE and RMSE, the scores of the proposed method are considerably lower than that of the compared methods. This result suggests that the surface information can be restored accurately in hazy regions and maintained well in clear regions. $\boldsymbol{R}^2$ shows that the score of the proposed method

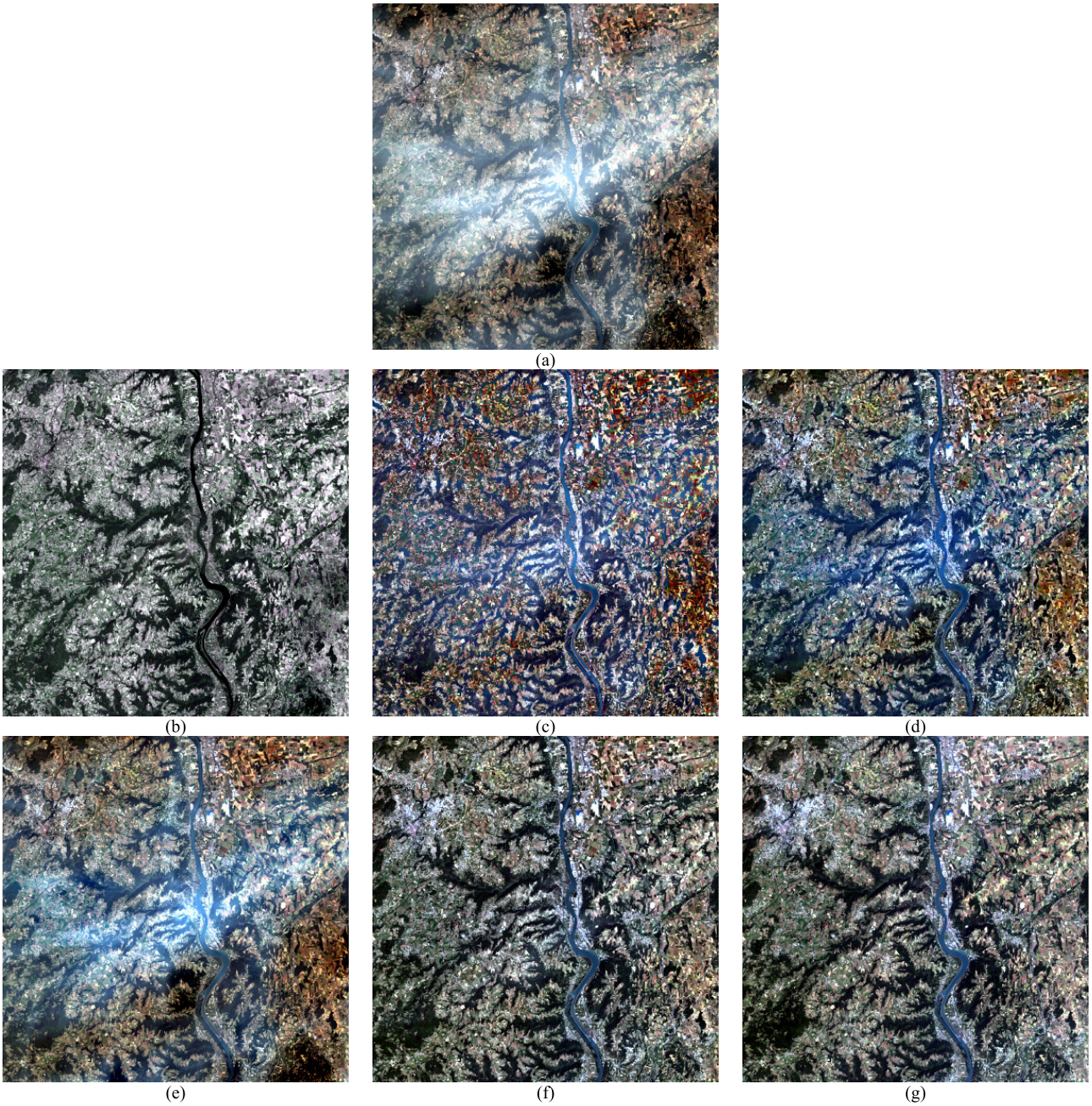

Fig. 5. Haze removal results for a synthetic image based on Landsat-8 OLI. (a) Synthetic image. (b) HOT. (c) FVR. (d) TDCP. (e) DSP. (f) Proposed method. (g) Ground truth.

is up to 0.9477, which indicates that the restored information in each band is highly consistent with that of the ground truth. Furthermore, SA of the proposed method is 0.5872, which is considerably lower than that of the other methods. That is, the spectral difference between the result and the ground truth is extremely small. All quantitative assessments suggest that the proposed method is effective in accurately correcting hazy ground information and considerably maintaining the clear regions.

Another synthetic hazy image was generated based on GaoFen-1 WFV with a 16-m spatial resolution [see Fig. 6(a)]. Fig. 6(b)–(f) shows the haze removal results using a variety of methods. Fig. 6(g) illustrates the ground truth. Fig. 6(b) shows that HOT removes most haze over the entire scene while residuals remain. That is because the land covers of the clearly referenced regions are different from those of the hazy regions, thereby leading to inaccuracy in the estimated HOT map. The results of FVR, TDCP, and DSP show a similar performance with the result in Fig. 5. For the result of the proposed method, all the haze is removed and the entire image is substantially approximating the ground truth.

Table II presents the four metrics calculated. For the result of FVR, the scores are the worst in all metrics, which are similar to previous synthetic experiments. Compared with

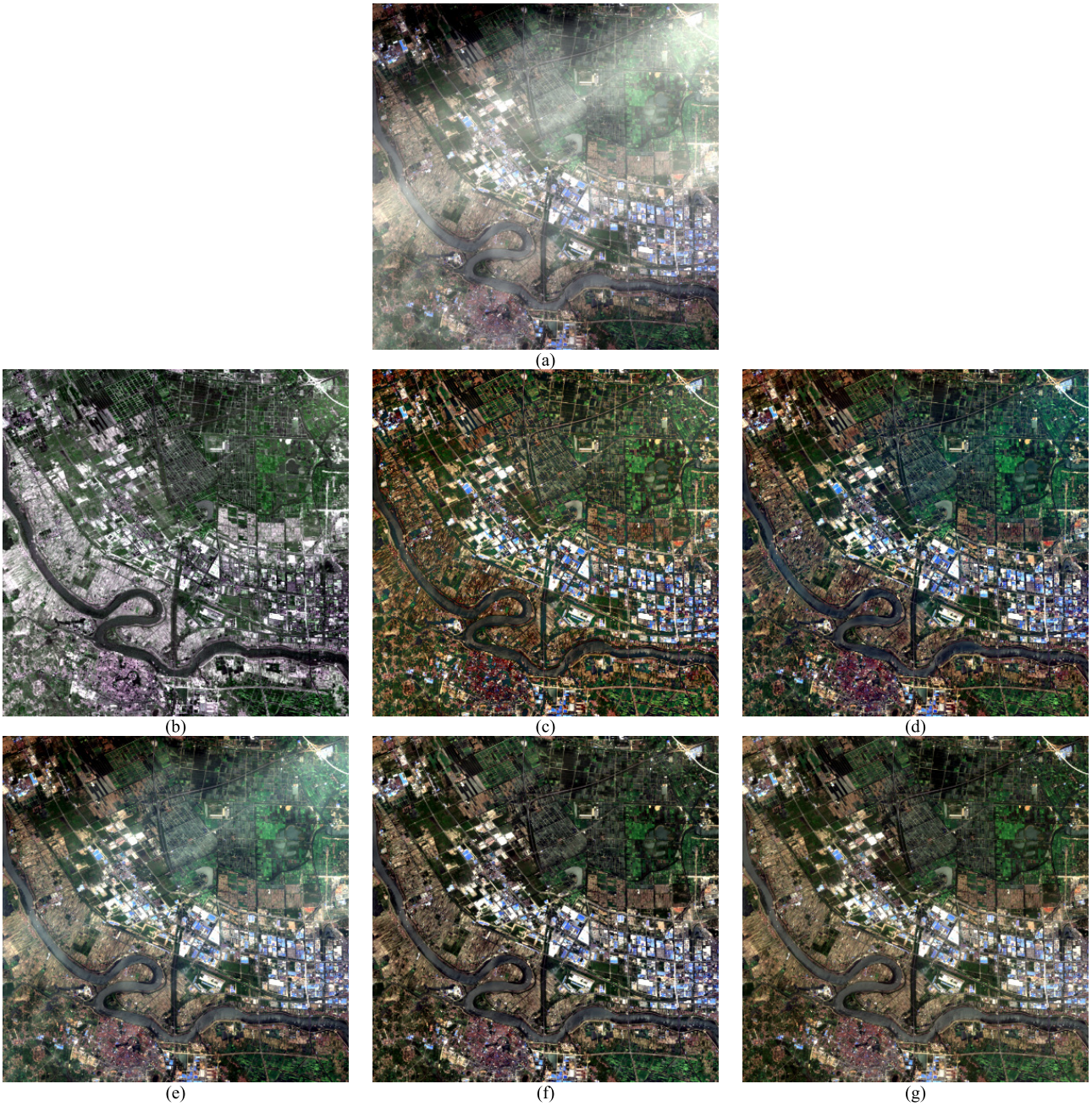

Fig. 6. Haze removal results for a synthetic image based on GaoFen-1 WFV. (a) Synthetic image. (b) HOT. (c) FVR. (d) TDCP. (e) DSP. (f) Proposed method. (g) Ground truth.

TABLE II
QUANTITATIVE ASSESSMENT OF DIFFERENT RESULTS

	HOT	FVR	TDCP	DSP	Proposed
MAE	7.1408	12.5122	5.2857	5.5021	**2.2689**
R^2	0.4776	0.8080	0.8915	0.7812	**0.9455**
RMSE	9.3986	13.6252	6.2720	6.3337	**2.9346**
SA	2.6310	5.3177	3.2054	3.8166	**1.2741**

FVR, the scores of HOT are evidently improved. The scores of TDCP and DSP show that all the metrics indicate better performance compared with those in the previous methods. For the result of the proposed method, MAE, RMSE, and SA are the lowest, and $\boldsymbol{R^2}$ is the closest to 1. Accordingly, the result approaches the ground truth.

C. Real-Data Experiments

Fig. 7(a) shows a hazy image cropped from a forest area, which also contains large areas of bare soil and is characterized by uneven haze. The results of the different methods are shown in Fig. 7(b)–(f). For the result of HOT, the color of the entire image is distorted and the details are blurred [see Fig. 7(b)]. The FVR result is shown in Fig. 7(c), which illustrates that the dense haze and light haze are eliminated completely, and the contrast of the entire image is enhanced.

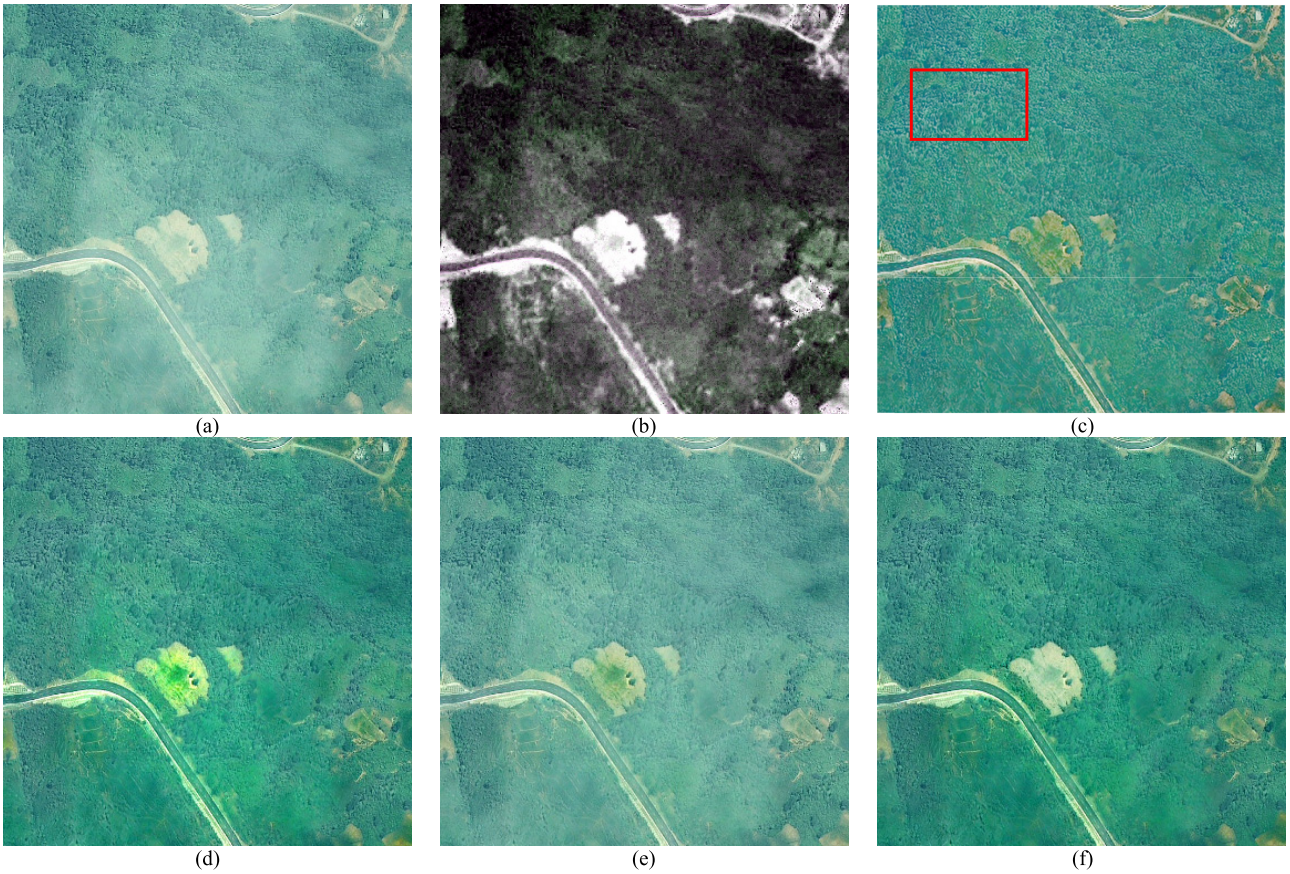

Fig. 7. Haze removal results for a forest image. (a) Hazy image. (b) HOT. (c) FVR. (d) TDCP. (e) DSP. (f) Proposed method.

Nevertheless, the result suffers from significant overcorrection, particularly in the bare-soil areas. Moreover, halo artifacts appear near the discontinuities owing to the "median of median filter" adopted in FVR [43] [see red rectangle in Fig. 7(c)]. Fig. 7(d) shows that the TDCP result is substantially better than the previous results, but part of haze remains and bare-soils are also overcorrected. Visually, the influence of haze is partially weakened by DSP, and the image details are enhanced, although some haze remains. In addition, the color of the bare soils is evidently distorted owing to the invalidation of the saturation prior to such a noncolorful scene, as shown in Fig. 7(e). Differing from the other results, the bare-soil areas are treated appropriately in the proposed method, and the haze influence in the visible bands is successfully removed [see Fig. 7(f)]. That is, the proposed method can faithfully recover color and significantly enhance the image details occluded by haze.

Fig. 8(a) shows a hazy bare land image, including abundant bare soils and some vegetation. Fig. 8(b)–(f) shows the results of the different methods. For the HOT result, nearly all haze is removed and the color is maintained substantially, although many texture details are blurred. Similar to the result of the previous experiment, the majority of the haze is successfully removed using FVR, whereas image color is distorted after the correction [see Fig. 8(c)]. TDCP maintains the general color of the image, but the haze is partially removed, as can be seen in Fig. 8(d). DSP has the same problem as TDCP. That is, haze cannot be removed completely, as can be observed from Fig. 8(e). For the result of the proposed method, all haze is successfully removed and the color of the dehazed regions is consistent with the clear regions. This result indicates that the haze influence in the spectral and spatial dimensions is eliminated, and the degraded information is recovered accurately using the proposed method.

Fig. 9(a) shows a coastal image containing a uniform haze and a large area of bright mudflats. Uniform haze can be easily removed by all the methods, but the large area of bright mudflats is a challenge. Note that the experimental data are cropped from a large image, and the clear regions required in HOT can be obtained from the remainder of the large image. The results of the different methods are shown in Fig. 9(b)–(f). The HOT result shows that the color of the entire scene is clearly distorted. For example, the water region is substantially darker than it should be. The FVR result shows that haze is removed completely, but the result suffers from significant overcorrection, particularly in the bright mudflat area. The TDCP result has the same problem as that of FVR (i.e., bright regions are overcorrected). The DSP result indicates that the color of the bare-soils is distorted, and the water surface is substantially darker than the surroundings, as shown in Fig. 9(e). The result of the proposed method is presented in Fig. 9(f), where the haze is eliminated considerably and

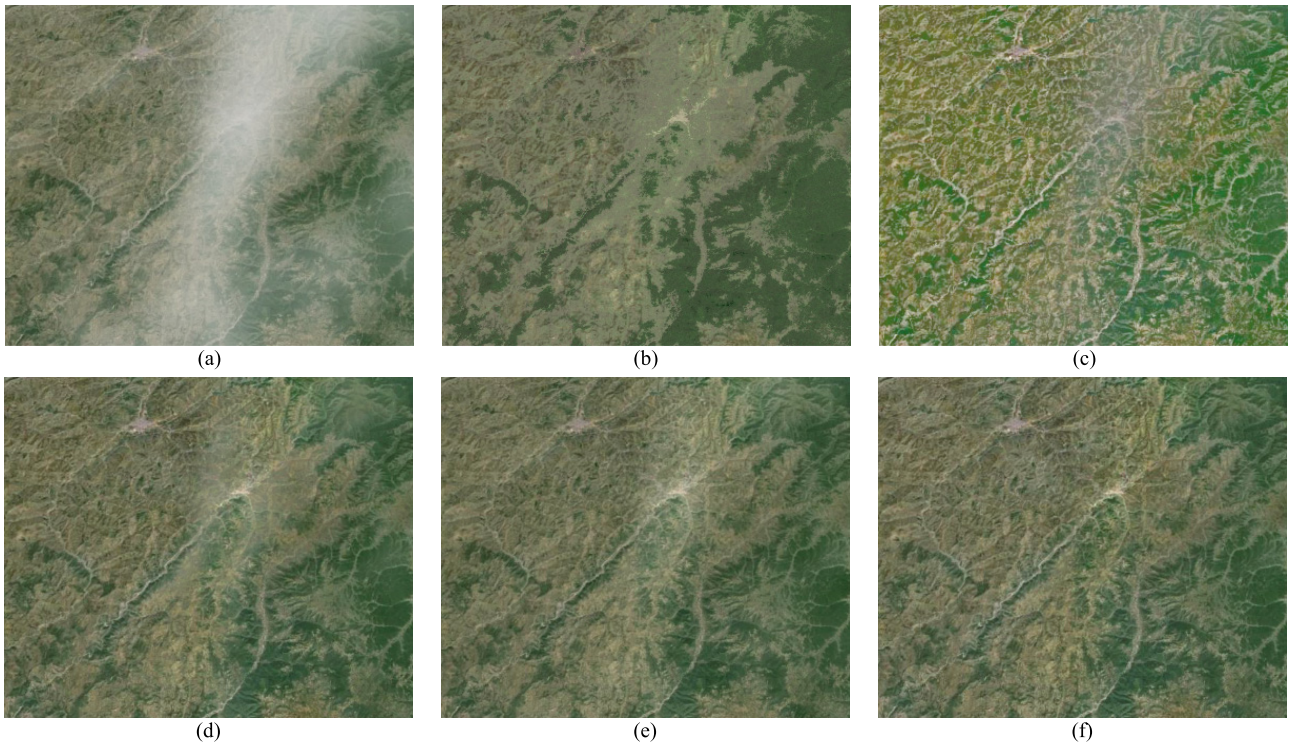

Fig. 8. Haze removal results for a bare land image. (a) Hazy image. (b) HOT. (c) FVR. (d) TDCP. (e) DSP. (f) Proposed method.

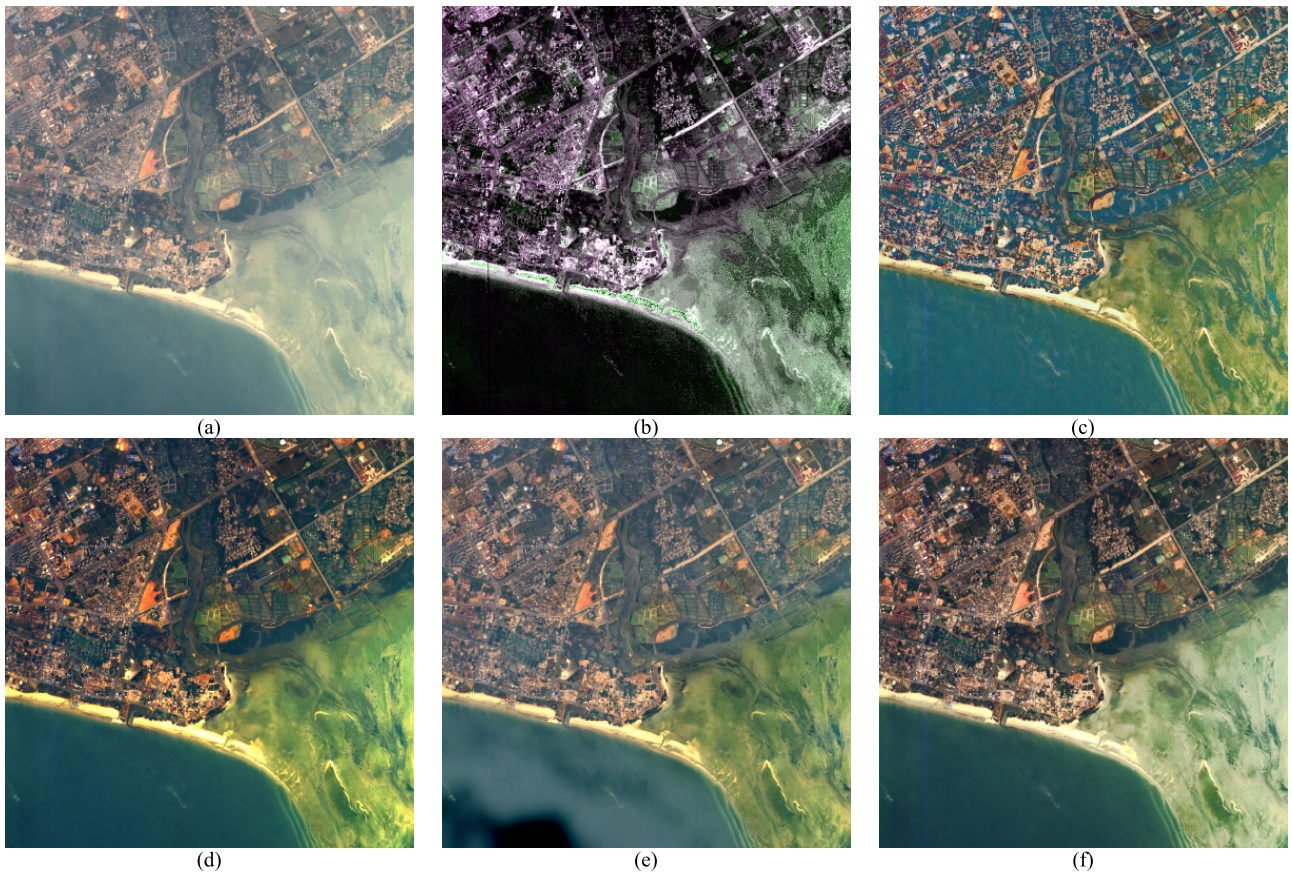

Fig. 9. Haze removal results for a coastal image. (a) Hazy image. (b) HOT. (c) FVR. (d) TDCP. (e) DSP. (f) Proposed method.

the image color is consistent with that of the original image. Moreover, for the large bright mudflat area, the proposed method can handle it correctly and recover the color faithfully.

A pair of hazy and clear images was collected to further quantitatively investigate the haze removal ability of the proposed method for real hazy image. The hazy and clear images

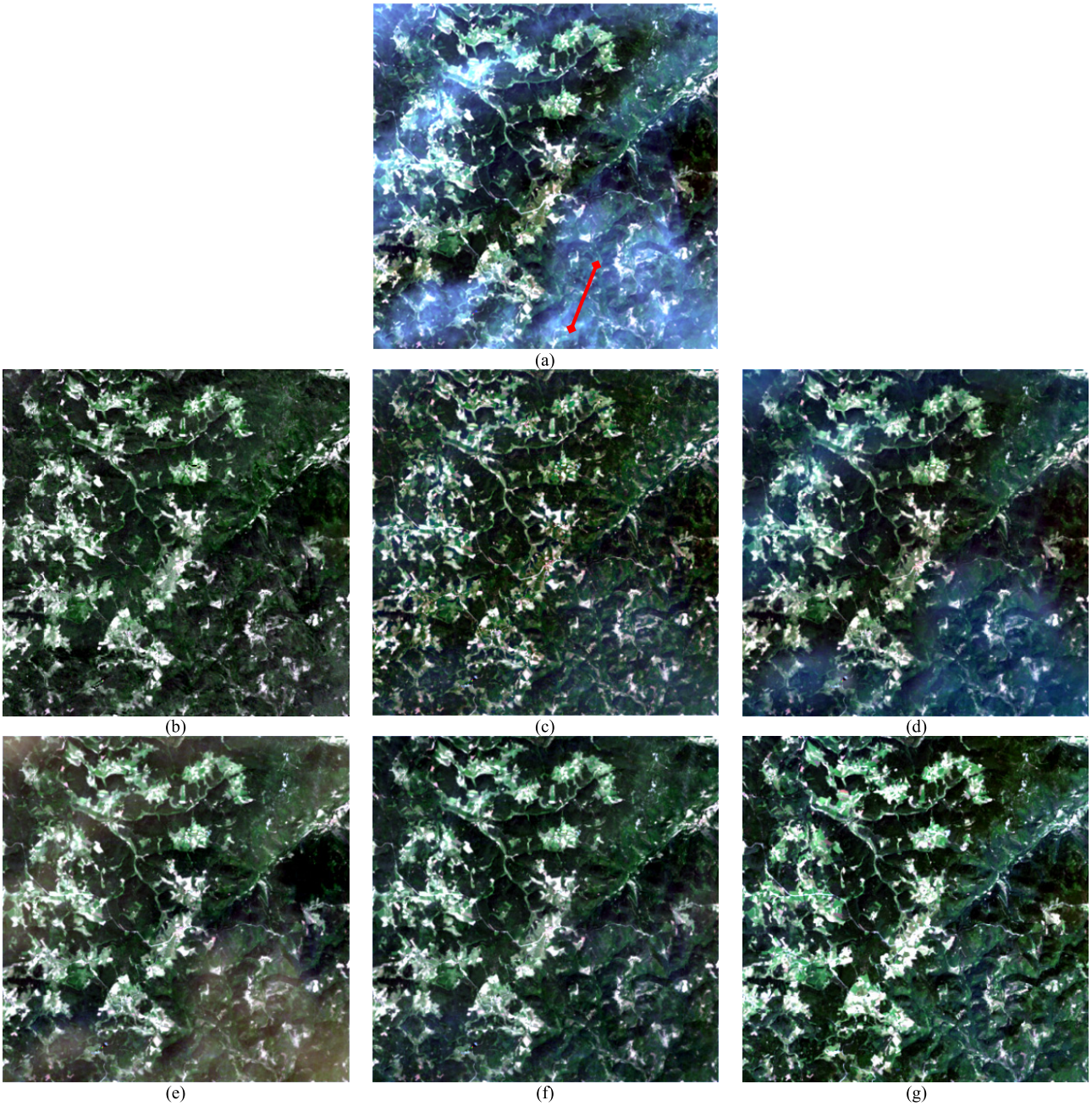

Fig. 10. Comparison to a haze-free reference image. (a) Hazy image. (b) HOT. (c) FVR. (d) TDCP. (e) DSP. (f) Proposed method. (g) Reference image.

were captured by OLI on July 1 and 17, 2014, respectively. The time interval of the two images is 16 days, a revisit period of OLI. Thus, the temporal variation of the ground surface was the smallest and can be disregarded, thereby enabling us to use the clear image as a reference [25], [28]. Moreover, the evaluations of the proposed method were performed through a comparison of the spectra and data consistencies.

Fig. 10(a) shows the hazy image acquired in a mountainous area. Evidently, the image includes vegetation, bare soil, and uneven haze. Fig. 10(b)–(f) shows the results of HOT, FVR, TDCP, DSP, and the proposed method, respectively. Fig. 10(e) presents the haze-free reference image acquired from the neighbor revisit period. Similar to previous real-data experiments, HOT and FVR can completely remove haze but can cause a slight color drift after the correction, as shown in Fig. 10(b) and (c). TDCP and DSP substantially maintain the color of the original clear regions, but the results contain residual haze leading to color distortion. For the proposed method, all haze can be completely removed, and the restored image is visually closest to the reference image.

A line that travels through the hazy regions was selected, as marked in red in Fig. 10(a). The mean profile curves of the visible bands are illustrated in Fig. 11. The curves of the different results are lower than that of the original hazy image, thereby indicating that the high brightness caused by haze is eliminated by these methods. Among these curves, the curve

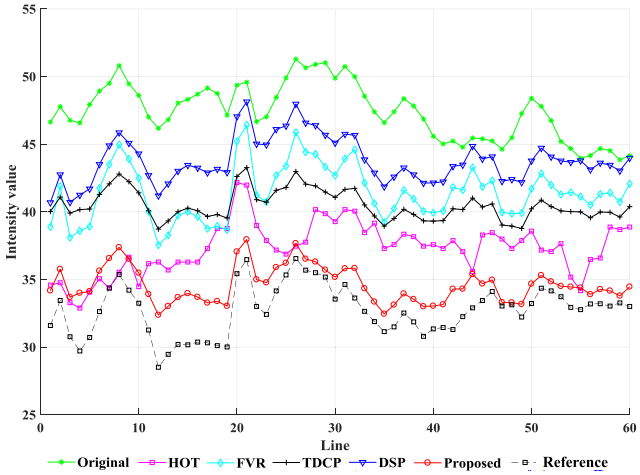

Fig. 11. Comparison of mean radiance profile curves between different results and the reference image.

TABLE III
QUANTITATIVE ASSESSMENT OF DIFFERENT RESULTS

	HOT	FVR	TDCP	DSP	Proposed
R^2	0.8809	0.9139	0.9168	0.8705	**0.9258**
SSIM	0.8591	0.8056	0.8514	0.8214	**0.8903**
CC	0.7772	0.7650	0.7919	0.7890	**0.8215**

of the proposed method is the lowest and is the closest to the reference image. That is, haze is removed properly and the restored information is highly consistent with the reference data. The reason why the two curves do not overlap completely is due to phenological changes and the varying atmospheric conditions. By analyzing the curve shapes, the result of the proposed method is similar to the original hazy image, thereby indicating that the spectra of the hazy regions are recovered faithfully while removing the haze.

Three metrics, $\boldsymbol{R^2}$, SSIM, and CC, were calculated to further assess the data consistency between the different results and the reference image. The closer the metric to 1, the higher the consistency of the two images. The calculation formulas of SSIM and CC are as follows [41], [44]:

$$\text{SSIM} = \frac{\left(2\bar{J}\bar{\hat{J}} + c_1\right)\left(2\text{cov}_{J\hat{J}} + c_2\right)}{\left(\bar{J}^2 + \bar{\hat{J}}^2 + c_1\right)\left(\mu_J^2 + \mu_{\hat{J}}^2 + c_2\right)} \tag{18}$$

$$\text{CC} = \frac{\text{cov}_{J\hat{J}}}{\mu_J \mu_{\hat{J}}} \tag{19}$$

where cov is the covariance, μ is the standard deviation, and c_1 and c_2 are the constants that prevent the denominator from being 0.

Table III shows the average scores of the visible bands for these results. Obviously, all scores of the proposed method are higher than the other four and are the closest to 1. This result indicates that the restored image is highly consistent with the reference image.

The synthetic and real-data experiments indicate that the proposed method is effective in removing haze for various scenes. However, the proposed method would show limited performance when the haze intensity is high and seriously occludes surface information.

V. CONCLUSION

This article proposed a spatial–spectral adaptive haze removal method for single visible remote sensing images. Three innovations play important roles in ensuring the haze removal performance. First, the nonuniform atmospheric light model describes the variation of atmospheric scattering in the global scene to effectively remove uneven haze contamination. Second, spatial correction for the transmission based on BPI identification overcomes the underestimation of the TDCP method and makes the proposed method more suitable for complex scenes. Third, the relationship between gradient and transmission is maximized to adaptively calculate transmission according to the atmospheric scattering characteristic, which effectively maintains the color and spectral features of the data. Multiple visible remotely sensed images acquired from different atmospheric conditions and scenes were collected to perform synthetic and real-data experiments, thereby validating the universality and effectiveness of the proposed method. Visually, the proposed method was able to completely remove haze, and could faithfully restore image colors and details. Quantitatively, the results held superior performance in all metrics compared with the other methods. In addition, the profile curve of our result is the most consistent with that of the reference data, thereby verifying the spectral preservation and recovery abilities of the proposed method. Overall, the proposed method outperformed the four comparison methods, and is efficient for use with single remote sensing images with different scenes and various types of haze.

REFERENCES

[1] H. Shen *et al.*, "Missing information reconstruction of remote sensing data: A technical review," *IEEE Geosci. Remote Sens. Mag.*, vol. 3, no. 3, pp. 61–85, Sep. 2015.
[2] R. Richter, "Atmospheric correction of satellite data with haze removal including a haze/clear transition region," *Comput. Geosci.*, vol. 22, no. 6, pp. 675–681, Jul. 1996.
[3] R. Fattal, "Dehazing using color-lines," *ACM Trans. Graph.*, vol. 34, no. 1, pp. 1–14, Dec. 2014.
[4] S. Chen, X. Chen, J. Chen, P. Jia, X. Cao, and C. Liu, "An iterative haze optimized transformation for automatic cloud/haze detection of Landsat imagery," *IEEE Trans. Geosci. Remote Sens.*, vol. 54, no. 5, pp. 2682–2694, May 2016.
[5] Q. Cheng, H. Shen, L. Zhang, Q. Yuan, and C. Zeng, "Cloud removal for remotely sensed images by similar pixel replacement guided with a spatio-temporal MRF model," *ISPRS J. Photogramm. Remote Sens.*, vol. 92, pp. 54–68, Jun. 2014.
[6] Y. Du, B. Guindon, and J. Cihlar, "Haze detection and removal in high resolution satellite image with wavelet analysis," *IEEE Trans. Geosci. Remote Sens.*, vol. 40, no. 1, pp. 210–217, Jan. 2002.
[7] M. Xu, X. Jia, and M. Pickering, "Cloud effects removal via sparse representation," in *Proc. IEEE Int. Geosci. Remote Sens. Symp. (IGARSS)*, Jul. 2015, pp. 605–608.
[8] M. Xu, X. Jia, M. Pickering, and A. J. Plaza, "Cloud removal based on sparse representation via multitemporal dictionary learning," *IEEE Trans. Geosci. Remote Sens.*, vol. 54, no. 5, pp. 2998–3006, May 2016.
[9] H. Li, L. Zhang, H. Shen, and P. Li, "A variational gradient-based fusion method for visible and SWIR imagery," *Photogramm. Eng. Remote Sens.*, vol. 78, no. 9, pp. 947–958, Sep. 2012.
[10] Y. J. Kaufman and C. Sendra, "Algorithm for automatic atmospheric corrections to visible and near-IR satellite imagery," *Int. J. Remote Sens.*, vol. 9, no. 8, pp. 1357–1381, Aug. 1988.

[11] S. Liang, H. Fallah-Adl, S. Kalluri, J. Jájá, Y. J. Kaufman, and J. R. G. Townshend, "An operational atmospheric correction algorithm for landsat thematic mapper imagery over the land," *J. Geophys. Res., Atmos.*, vol. 102, no. D14, pp. 17173–17186, Jul. 1997.

[12] R. Richter, "Some aspects of the atmospheric radiance model of LOWTRAN 6," *Int. J. Remote Sens.*, vol. 6, no. 11, pp. 1773–1777, Nov. 1985.

[13] W. Zhao, M. Tamura, and H. Takahashi, "Atmospheric and spectral corrections for estimating surface albedo from satellite data using 6S code," *Remote Sens. Environ.*, vol. 76, no. 2, pp. 202–212, May 2001.

[14] S. Liang, H. Fang, and M. Chen, "Atmospheric correction of Landsat ETM+ land surface imagery. I. Methods," *IEEE Trans. Geosci. Remote Sens.*, vol. 39, no. 11, pp. 2490–2498, Nov. 2001.

[15] S. Liang *et al.*, "Atmospheric correction of Landsat ETM+ land surface imagery. II. Validation and applications," *IEEE Trans. Geosci. Remote Sens.*, vol. 40, no. 12, pp. 2736–2746, Dec. 2002.

[16] H. Shen, H. Li, Y. Qian, L. Zhang, and Q. Yuan, "An effective thin cloud removal procedure for visible remote sensing images," *ISPRS J. Photogramm. Remote Sens.*, vol. 96, pp. 224–235, Oct. 2014.

[17] J. Liu *et al.*, "Thin cloud removal from single satellite images," *Opt. Express*, vol. 22, no. 1, pp. 618–632, Jan. 2014.

[18] Y. Zhang, B. Guindon, and J. Cihlar, "An image transform to characterize and compensate for spatial variations in thin cloud contamination of Landsat images," *Remote Sens. Environ.*, vol. 82, nos. 2–3, pp. 173–187, Oct. 2002.

[19] C. Liu, J. Hu, Y. Lin, S. Wu, and W. Huang, "Haze detection, perfection and removal for high spatial resolution satellite imagery," *Int. J. Remote Sens.*, vol. 32, no. 23, pp. 8685–8697, Dec. 2011.

[20] H. Jiang, N. Lu, and L. Yao, "A high-fidelity haze removal method based on HOT for visible remote sensing images," *Remote Sens.*, vol. 8, no. 10, p. 844, Oct. 2016.

[21] E. P. Crist and R. C. Cicone, "A physically-based transformation of thematic mapper data—The TM tasseled cap," *IEEE Trans. Geosci. Remote Sens.*, vols. GRS-22, no. 3, pp. 256–263, May 1984.

[22] J. Lavreau, "De-hazing Landsat thematic mapper images," *Photogramm. Eng. Remote Sens.*, vol. 57, no. 10, pp. 1297–1302, Oct. 1991.

[23] Y. Shen, Y. Wang, H. Lv, and J. Qian, "Removal of thin clouds in Landsat-8 OLI data with independent component analysis," *Remote Sens.*, vol. 7, no. 9, pp. 11481–11500, Sep. 2015.

[24] M. Xu, X. Jia, M. Pickering, and S. Jia, "Thin cloud removal from optical remote sensing images using the noise-adjusted principal components transform," *ISPRS J. Photogramm. Remote Sens.*, vol. 149, pp. 215–225, Mar. 2019.

[25] H. Lv, Y. Wang, and Y. Shen, "An empirical and radiative transfer model based algorithm to remove thin clouds in visible bands," *Remote Sens. Environ.*, vol. 179, pp. 183–195, Jun. 2016.

[26] R. K. Vincent, "An ERTS multispectral scanner experiment for mapping iron compounds," in *Proc. 8th Int. Symp. Remote Sens. Environ.*, Ann Arbor, MI, USA, 1972, pp. 1239–1247.

[27] P. S. Chavez, Jr., "An improved dark-object subtraction technique for atmospheric scattering correction of multispectral data," *Remote Sens. Environ.*, vol. 24, no. 3, pp. 459–479, Apr. 1988.

[28] A. Makarau, R. Richter, R. Müller, and P. Reinartz, "Haze detection and removal in remotely sensed multispectral imagery," *IEEE Trans. Geosci. Remote Sens.*, vol. 52, no. 9, pp. 5895–5905, Sep. 2014.

[29] K. He, J. Sun, and X. Tang, "Single image haze removal using dark channel prior," *IEEE Trans. Pattern Anal. Mach. Intell.*, vol. 33, no. 12, pp. 2341–2353, Dec. 2011.

[30] H. Jiang, N. Lu, L. Yao, and X. Zhang, "Single image dehazing for visible remote sensing based on tagged haze thickness maps," *Remote Sens. Lett.*, vol. 9, no. 7, pp. 627–635, Jul. 2018.

[31] J. Long, Z. Shi, W. Tang, and C. Zhang, "Single remote sensing image dehazing," *IEEE Geosci. Remote Sens. Lett.*, vol. 11, no. 1, pp. 59–63, Jan. 2014.

[32] X. Lan, L. Zhang, H. Shen, Q. Yuan, and H. Li, "Single image haze removal considering sensor blur and noise," *EURASIP J. Adv. Signal Process.*, vol. 2013, no. 1, p. 86, Dec. 2013.

[33] X. Pan, F. Xie, Z. Jiang, and J. Yin, "Haze removal for a single remote sensing image based on deformed haze imaging model," *IEEE Signal Process. Lett.*, vol. 22, no. 10, pp. 1806–1810, Oct. 2015.

[34] F. Xie, J. Chen, X. Pan, and Z. Jiang, "Adaptive haze removal for single remote sensing image," *IEEE Access*, vol. 6, pp. 67982–67991, 2018.

[35] P.-J. Liu, S.-J. Horng, J.-S. Lin, and T. Li, "Contrast in haze removal: Configurable contrast enhancement model based on dark channel prior," *IEEE Trans. Image Process.*, vol. 28, no. 5, pp. 2212–2227, May 2019.

[36] J. Li, Q. Hu, and M. Ai, "Haze and thin cloud removal via sphere model improved dark channel prior," *IEEE Geosci. Remote Sens. Lett.*, vol. 16, no. 3, pp. 472–476, Mar. 2019.

[37] R. Fattal, "Single image dehazing," *ACM Trans. Graph.*, vol. 27, no. 3, p. 72, Aug. 2008.

[38] S. G. Narasimhan and S. K. Nayar, "Vision and the atmosphere," *Int. J. Comput. Vis.*, vol. 48, no. 3, pp. 233–254, Jul. 2002.

[39] S. G. Narasimhan and S. K. Nayar, "Contrast restoration of weather degraded images," *IEEE Trans. Pattern Anal. Mach. Intell.*, vol. 25, no. 6, pp. 713–724, Jun. 2003.

[40] J.-P. Tarel and N. Hautiere, "Fast visibility restoration from a single color or gray level image," in *Proc. IEEE 12th Int. Conf. Comput. Vis.*, Sep. 2009, pp. 2201–2208.

[41] K. Muhammad, J. Ahmad, S. Rho, and S. W. Baik, "Image steganography for authenticity of visual contents in social networks," *Multimedia Tools Appl.*, vol. 76, no. 18, pp. 18985–19004, Sep. 2017.

[42] Y. Sohn and N. S. Rebello, "Supervised and unsupervised spectral angle classifiers," *Photogramm. Eng. Remote Sens.*, vol. 68, no. 12, pp. 1271–1282, Dec. 2002.

[43] Q. Zhu, J. Mai, and L. Shao, "A fast single image haze removal algorithm using color attenuation prior," *IEEE Trans. Image Process.*, vol. 24, no. 11, pp. 3522–3533, Nov. 2015.

[44] J. Benesty, J. Chen, Y. Huang, and I. Cohen, "Pearson correlation coefficient," in *Noise Reduction in Speech Processing*. Berlin, Germany: Springer, 2009, pp. 1–4.

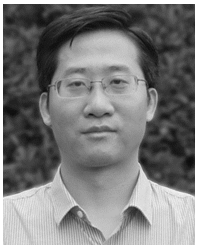

Huanfeng Shen (Senior Member, IEEE) received the B.S. degree in surveying and mapping engineering and the Ph.D. degree in photogrammetry and remote sensing from Wuhan University, Wuhan, China, in 2002 and 2007, respectively.

In 2007, he joined the School of Resource and Environmental Sciences, Wuhan University, where he is currently a Luojia Distinguished Professor. He is a "Chang-Jiang Scholar" Distinguished Professor appointed by the Ministry of Education of China with the School of Resource and Environmental Sciences, Wuhan University. He has authored more than 100 research articles. His research interests include image quality improvement, remote sensing mapping and application, data fusion and assimilation, and regional and global environmental change.

Dr. Shen is currently a member of the Editorial Board of the *Journal of Applied Remote Sensing*. He has been supported by several talent programs, such as the Youth Talent Support Program of China in 2015, the China National Science Fund for Excellent Young Scholars in 2014, and the New Century Excellent Talents by the Ministry of Education of China in 2011.

Chi Zhang received the B.S. degree in surveying and mapping engineering from Hohai University, Nanjing, China, in 2016. He is currently pursuing the Ph.D. degree in cartography and geographic information engineering with the School of Resource and Environmental Sciences, Wuhan University, Wuhan, China.

His research interests include the haze removal of optical remote sensing images.

Huifang Li (Member, IEEE) received the B.S. degree in geographical information science from the China University of Mining and Technology, Xuzhou, China, in 2008, and the Ph.D. degree in photogrammetry and remote sensing from Wuhan University, Wuhan, China, in 2013.

She is currently an Associate Professor with the School of Resources and Environmental Sciences, Wuhan University. She focuses on the study of radiometric correction of remote sensing images, including cloud correction, shadow correction, and urban thermal environment analysis and alleviation.

Quan Yuan received the B.S. degree in geographic information system and the M.S. degree in surveying and mapping engineering from Wuhan University, Wuhan, China, in 2014 and 2016, respectively.

He is currently a Researcher with Guangdong OPPO Mobile Telecommunications Corporation, Ltd., Dongguan, China. His research interest includes digital image processing.

Liangpei Zhang (Fellow, IEEE) received the B.S. degree in physics from Hunan Normal University, Changsha, China, in 1982, the M.S. degree in optics from the Xi'an Institute of Optics and Precision Mechanics, Chinese Academy of Sciences, Xi'an, China, in 1988, and the Ph.D. degree in photogrammetry and remote sensing from Wuhan University, Wuhan, China, in 1998.

He was a Principal Scientist for the China State Key Basic Research Project from 2011 to 2016 appointed by the Ministry of National Science and Technology of China to lead the Remote Sensing Program in China. He is a "Chang-Jiang Scholar" Chair Professor appointed by the Ministry of Education of China with State Key Laboratory of Information Engineering in Surveying, Mapping, and Remote Sensing (LIESMARS), Wuhan University. He has published more than 700 research articles and five books. He holds 30 patents. His research interests include hyperspectral remote sensing, high-resolution remote sensing, image processing, and artificial intelligence.

Dr. Zhang is a fellow of the Institution of Engineering and Technology (IET). He was a recipient of the 2010 Best Paper Boeing Award, the 2013 Best Paper ERDAS Award from the American Society of Photogrammetry and Remote Sensing (ASPRS), and the 2016 Best Paper Theoretical Innovation Award from the International Society for Optics and Photonics (SPIE). His research teams won the top three prizes of the IEEE GRSS 2014 Data Fusion Contest, and his students have been selected as the winners or finalists of the IEEE International Geoscience and Remote Sensing Symposium (IGARSS) Student Paper Contest in recent years. He also serves as an Associate Editor and an Editor for more than ten international journals. He is currently serving as an Associate Editor for the IEEE TRANSACTIONS ON GEOSCIENCE AND REMOTE SENSING. He is the Founding Chair of IEEE Geoscience and Remote Sensing Society (GRSS) Wuhan Chapter. He is the Institute for Scientific Information (ISI) highly cited author.